ADVANCED FUNCTIONAL MATERIALS
www.afm-journal.de

Atomically Thin Decoration Layers for Robust Orientation Control of 2D Transition Metal Dichalcogenides

Yu-Ming Chang, Ni Yang, Jiacheng Min, Fangyuan Zheng, Chun-Wei Huang, Jui-Yuan Chen, Yuxiang Zhang, Pengfei Yang, Chenyang Li, Hao-Yu Liu, Beilin Ye, Jian-Bin Xu, Han-Yi Chen, Zhengtang Luo, Wen-Wei Wu, Kaimin Shih, Jing-Kai Huang, Lain-Jong Li, and Yi Wan**

2D semiconducting transition metal dichalcogenides (TMDs) are emerging as promising candidates in the pursuit of advancing semiconductor technology. One major challenge for integrating 2D TMD materials into practical applications is developing an epitaxial technique with robust reproducibility for single-oriented growth and thus single-crystal growth. Here, the growth of single-orientated MoS_2 on c-plane sapphire with atomically thin Fe_2O_3 decoration layers under various growth conditions is demonstrated. The statistical data highlight robust reproducibility, achieving a single orientation ratio of up to 99%. Density functional theory calculations suggest that MoS_2 favors a 0° alignment ([11$\bar{2}$0]// [11$\bar{2}$0]) on the Fe_2O_3 (0001) surface. This preference ensures single-oriented growth, even on mirror-reflected exposed surfaces which typically lead to antiparallel domains. Subsequent optical and electrical analyses confirm the uniformity and undoped nature of MoS_2 on Fe_2O_3-decorated sapphire, showing its quality is comparable to MoS_2 grown on bared sapphires. The results underscore the potential of Fe_2O_3-decorated sapphire as an effective substrate for the consistent and high-quality epitaxial growth of 2D TMDs, illuminating the pathway to epitaxial control of 2D TMD orientation through strategic modulation of crystalline atomic surfaces.

1. Introduction

The achievement of wafer-scale growth of single crystal 2D semiconducting transition metal dichalcogenide (TMD) materials holds significant importance as it underpins the development of next-generation 2D field-effect transistor (FET) applications.[1] In the pursuit of synthesizing single crystal 2D TMD materials, chemical vapor deposition (CVD) emerges as a highly effective method, ensuring scalability and reproducibility for large-scale manufacturing.[2] One crucial aspect of this growth process is the selection and modification of substrates, which serve as seed layers for guiding the nucleation process. In recent developments, significant progress has been made in demonstrating single-oriented TMD materials on various substrates with specific symmetry and controlled surface steps.[2b,3] However, it is essential to note that the growth orientation

Y.-M. Chang, N. Yang, F. Zheng, P. Yang, C. Li, B. Ye, L.-J. Li, Y. Wan
Department of Mechanical Engineering
The University of Hong Kong
Hong Kong China
E-mail: lanceli1@hku.hk; wanyi@hku.hk

J. Min, K. Shih
Department of Civil Engineering
The University of Hong Kong
Hong Kong China

C.-W. Huang
Department of Materials Science and Engineering
Feng Chia University
No. 100, Wenhua Rd., Xitun Dist., Taichung 407102, Taiwan

J.-Y. Chen
Department of Materials Science and Engineering
National United University
No. 2, Lienda, Miaoli City, Miaoli County 360302, Taiwan

Y. Zhang
Department of Electrical and Electronic Engineering
The University of Hong Kong
Hong Kong China

H.-Y. Liu, H.-Y. Chen
Department of Materials Science and Engineering
National Tsing Hua University
Hsinchu 300044, Taiwan

J.-B. Xu
Department of Electronic Engineering
The Chinese University of Hong Kong
Hong Kong China

The ORCID identification number(s) for the author(s) of this article can be found under https://doi.org/10.1002/adfm.202311387

© 2023 The Authors. Advanced Functional Materials published by Wiley-VCH GmbH. This is an open access article under the terms of the Creative Commons Attribution License, which permits use, distribution and reproduction in any medium, provided the original work is properly cited.

DOI: 10.1002/adfm.202311387

16163028, 2024, 10, Downloaded from https://onlinelibrary.wiley.com/doi/10.1002/adfm.202311387, Wiley Online Library on [26/09/2024]. See the Terms and Conditions (https://onlinelibrary.wiley.com/terms-and-conditions) on Wiley Online Library for rules of use; OA articles are governed by the applicable Creative Commons License

of 2D TMD materials can be influenced by various factors, giving rise to different mechanisms.[4] For example, intentionally creating stepped surfaces was found to be advantageous by providing favorable docking sites that enhance the energy discrepancy between antiparallel layers, leading to single-oriented 2D TMD materials growth on Au (111)[5] and sapphire surfaces.[2b,3c,6] Conversely, a statistical analysis has revealed that 88% of MoS_2 nuclei on Au(111) exhibit surface terrace nucleation following van der Waals epitaxy.[7] Coincidentally, our recent work underscores that uncontrolled steps on the *c*-plane of sapphire can produce mirror-reflected exposed surfaces, subsequently resulting in the formation of antiparallel MoS_2 flakes during growth.[6] In this context, the refinement of exposed surfaces is likely a more dominant factor than step–edge formation in controlling the growth orientation of 2D materials. In addition, experimental evidence has substantiated that the gas sources at high growth temperatures can react with the surface atoms of the substrate, forming a chalcogen or transition metal passivation layer, which in turn changes the preferred alignments of the TMD grains.[3b,8] The interplay between substrate surface steps, surface symmetry, and interfacial reconstructed layers creates a competitive environment where the single crystal epitaxy process of 2D materials can only be achieved under precisely manipulated growth conditions. Therefore, there is a demand for a commercially viable substrate that can effectively mitigate the competition between various factors, thereby enabling a higher percentage and improved reproducibility of single-orientation TMD grains.

Here, we developed an alternative approach by introducing atomically thin crystalline Fe_2O_3 (0001) decoration layers on commercially available *c*-plane sapphire substrates, enabling the realization of single orientation epitaxial growth of 2D MoS_2 under diverse growth conditions. Our simulation results validated that a 0° alignment ($[11\bar{2}0]//[11\bar{2}0]$) between MoS_2 layers and Fe_2O_3 (0001) is energetically favorable, which ensures the maintenance of single orientation alignment even on mirror-reflected exposed surfaces. Cross-section transmission electron microscopy (TEM) images demonstrate the high crystallinity and sustainability of the decorated Fe_2O_3 layers after the epitaxial growth of MoS_2. Moreover, a systematic investigation of the influence of growth conditions on MoS_2 orientation control has showcased the high reproducibility and a high percentage (≈99%) of single orientation alignment across various growth conditions. The field-effect transistors (FET) fabricated using as-grown single-oriented MoS_2 exhibit comparable electrical performance as MoS_2 grown on standard sapphire substrates, showing no evidence of doping effect from Fe.

Z. Luo
Department of Chemical and Biological Engineering
The Hong Kong University of Science and Technology
Hong Kong China
W.-W. Wu
Department of Materials Science and Engineering
National Yang Ming Chiao Tung University
Hsinchu 300093, Taiwan
J.-K. Huang
Department of Systems Engineering
City University of Hong Kong
Hong Kong China

2. Results and Discussion

Figure 1a schematically illustrates the experimental process. The Fe_2O_3-decorated c-plane sapphire was initially prepared through a process involving the spin-coating of $FeCl_{2(EtOH)}$, followed by annealing in an ambient atmosphere. In parallel, a control sample of bare c-plane sapphire was similarly annealed under identical conditions, serving as a comparison. This study used standard C-sapphire wafers featuring a miscut angle of 0.2°±0.1° towards the *M*-axis $[1\bar{1}00]$ (denoted as C/M sapphire). These wafers are primarily available in the market. Figure 1b,c present the Atomic Force Microscopy (AFM) images of the Fe_2O_3-decorated sapphire and annealed C/M sapphire surfaces, respectively. After annealing, C/M sapphire surfaces form sharp steps toward the *A*-axis $[11\bar{2}0]$ with a step height of 0.2 nm. In contrast, the forming of the Fe_2O_3 decoration layer leads to roughened surfaces devoid of precise step edges. The X-ray photoelectron spectroscopy (XPS) spectrum, as depicted in Figure S1 (Supporting Information), features a Fe $3d_{5/2}$ peak situated at 709.8 eV. This peak position is indicative of the formation of Fe_2O_3.[9] Subsequently, we used a low-pressure chemical vapor deposition (LPCVD, Figure S2, Supporting Information) process to synthesize MoS_2 monolayers. We observed that they formed in a single-oriented and antiparallel manner on the Fe_2O_3-decorated sapphire and annealed bare C/M sapphire substrates, respectively. Figure 1d and Figure S3 (Supporting Information) show the Scanning Electron Microscopy (SEM) and optical microscopy (OM) images respectively, highlighting the formation of highly single-oriented MoS_2 triangles on Fe_2O_3 decorated sapphire. Statistical analysis reveals a high single orientation occurrence of 98.9%. The Second Harmonic Generation (SHG) mapping is proven to detect grain boundaries effectively.[10] SHG images on MoS_2 triangles (Figure 1e) and films (Figure S4a,b, Supporting Information) demonstrate the absence of polycrystallinity and grain boundaries, whereas two orientations of antiparallel MoS_2 triangles were observed on the annealed C/M sapphire surfaces, as depicted in Figure S5 (Supporting Information). The antiparallel flakes with rotation angles of 30° and 90° grown on *c*-plane sapphire, which has a step height of 0.2 nm, are consistent with previous literature.[6] The single-crystal MoS_2 can reach a centimeter-scale size of ≈2 × 1 cm^2 large, as shown in Figure S4c (Supporting Information).

To assess the optical quality of the as-grown single-oriented MoS_2 monolayers on Fe_2O_3-decorated sapphire, we conducted Raman and photoluminescence (PL) spectrum analyses, as illustrated in **Figure 2a,b**. The E_{2g} and A_{1g} peaks of MoS_2 on Fe_2O_3-decorated sapphire were observed at 384.9 and 404.2 cm^{-1}, respectively, with a peak difference of 19.3 cm^{-1}, closely resembling the Raman peak of monolayer MoS_2 grown on annealed C/M sapphire.[2a,11] Simultaneously, the PL spectra for MoS_2 monolayers on both Fe_2O_3-decorated sapphire and annealed C/M sapphire exhibited similar positions at ≈1.87 eV, accompanied by a nearly identical full width at half maximum (FWHM) value of 62 meV. These findings indicate that both types of MoS_2 exhibit good quality, suggesting that MoS_2 grown on Fe_2O_3-decorated sapphire is on a par with that grown on annealed C/M sapphire.

Delving deeper into the chemical constitution of Mo and S within our sample, XPS was conducted on as-grown MoS_2. The resultant spectrum (Figure 2c) shows two peaks at 232.3 and 229 1 eV, indicating Mo^{4+} of $3d_{5/2}$ and $3d_{3/2}$, respectively.

© 2023 The Authors. Advanced Functional Materials published by Wiley-VCH GmbH

16163028, 2024, 10, Downloaded from https://onlinelibrary.wiley.com/doi/10.1002/adfm.202311387, Wiley Online Library on [26/09/2024]. See the Terms and Conditions (https://onlinelibrary.wiley.com/terms-and-conditions) on Wiley Online Library for rules of use; OA articles are governed by the applicable Creative Commons License

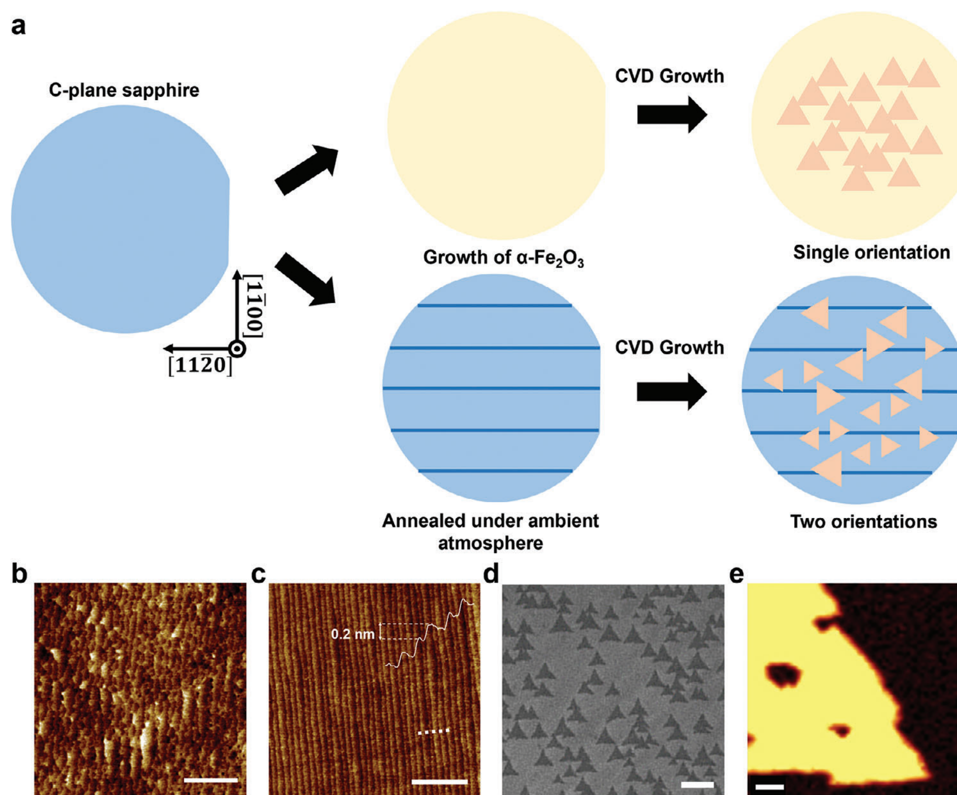

Figure 1. LPCVD growth of single-oriented MoS_2 on Fe_2O_3-decorated sapphire. a) Schematic illustration for the α-Fe_2O_3 decoration and MoS_2 growth. AFM images show the surface structures of b) Fe_2O_3-decorated sapphire and c) C/M sapphire (scale bar: 500 nm). d) SEM image of single-oriented MoS_2 (Scale bar: 10 µm). e) SHG mapping of single-crystal MoS_2 (scale bar: 1 µm).

Concurrently, the S 2s peak also shows in the spectrum located at 226.4 eV. S^{2-} $2p_{3/2}$ and $2p_{1/2}$ are located at 163.1 and 161.9 eV, respectively (Figure 2d).[12] Collectively, these spectral signatures resonate with the synthesis of MoS_2, characterized by Mo^{4+} and S^{2-} states.

It is worth highlighting that prior studies[13] have shown a pronounced Fe doping effect in single-orientated MoS_2 facilitated by $FeCl_2$. Interestingly, the MoS_2 growth achieved on Fe_2O_3-decorated sapphire exhibited no discernible shifts in both Raman and PL spectra, validating its innate undoped nature. In support of this, the top-view high-angle annular dark-field scanning transmission electron microscopy (HAADF-STEM) image presented in **Figure 3a** depicts a perfect honeycomb atomic arrangement. The absence of noticeable contrast variations in this arrangement underscores the high crystalline quality with fewer defects and dopants in as-grown MoS_2. Furthermore, the Energy Dispersive X-ray (EDX) mapping (Figure S6a, Supporting Information) and XPS analyses (Figure S6b, Supporting Information) from transferred MoS_2 samples revealed a negligible Fe signal, consolidating the conclusion that the as-grown MoS_2 samples were not doped with Fe-ions. One possible reason for this observation could be attributed to the high stability of the Fe_2O_3 decoration layers under higher growth temperatures.[14]

To reveal the epitaxial relationship between MoS_2 and sapphire, cross-sectional HAADF-STEM and EDX mapping were employed, as presented in Figure 3b,c. The EDX mapping images derived from cross-sectional TEM (Figure 3c) demonstrate the formation of atomically thin Fe_2O_3 layers on the sapphire surface. The cross-sectional HAADF-STEM image in Figure 3b shows a lattice spacing of 0.412 nm in Al_2O_3. This spacing perfectly corresponds to the $\sqrt{3}a_{Al_2O_3}/2$ ($\sqrt{3}/2 \times 0.481$ nm $= 0.412$ nm), implying that the Al_2O_3 (11$\bar{2}$0) plane is oriented outward. On the top of Al_2O_3, few-layer lattices with a corundum structure and elongated lattice distance of 0.439 nm indicate the formation of atomically thin α-Fe_2O_3 decoration layer ($\sqrt{3}a_{Fe_2O_3}/2 =$ 0.439 nm, $a_{Fe_2O_3} = 0.508$ nm).[2b,3c] It is noticeable that the lattice spacing of the top few layers does not match with Fe_2S_3 or any other sulfide analogs, which indicates that the sulfurization of Fe_2O_3 does not occur in this case. The lattice spacing of 0.274 nm ($\sqrt{3}/2 \times 0.316$ nm $= 0.274$ nm) on the top layer is measured, which corresponds to the MoS_2 armchair (AC, [1$\bar{1}$00]) direction. Herein, the growth orientation of MoS_2 along the [11$\bar{2}$0] axis is observed to be parallel to the direction of Fe_2O_3/Al_2O_3 [11$\bar{2}$0] on the Fe_2O_3-decorated sapphire substrates. This preferred growth orientation is perpendicular to that of C/M sapphire, as shown in **Figure 4a**.

Density function theory (DFT) calculations are widely used to discuss the detailed mechanism of 2D materials on various substrates.[2d,3b,5,6,8a,b] To elucidate the effect of Fe_2O_3 decoration layers, we conducted DFT calculations to determine the adsorption energy of MoS_2 on an ideal (0001) Al_2O_3–OH surface, as well as on (0001) Fe_2O_3 surface, since the DFT calculations are widely used to discuss the orientation of TMDs on various substrates.

© 2023 The Authors. Advanced Functional Materials published by Wiley-VCH GmbH

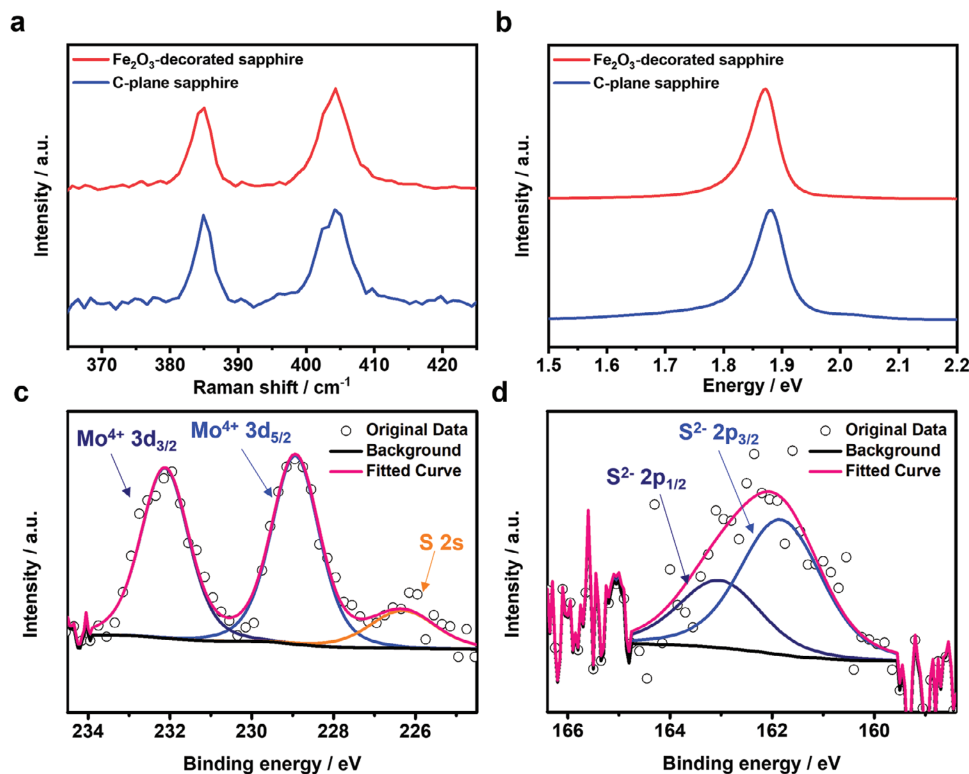

Figure 2. The properties of MoS_2. a) Raman and b) PL spectra of MoS_2 grown on Fe_2O_3-decorated sapphire (red line) and annealed C/M sapphire (blue line). c) Mo 3d spectrum of MoS_2 grown on Fe_2O_3-decorated sapphire. d) S 2p spectrum of MoS_2 grown on Fe_2O_3-decorated sapphire.

The choice of the Al_2O_3–OH surface is predicated upon empirical evidence showcasing its high stability.[15] The atomic configurations of these heterostructures are shown in Figure S7 (Supporting Information), where 0° represents the triangular MoS_2 [11$\bar{2}$0] edge aligned with the *A*-axis [11$\bar{2}$0] of sapphire. As depicted in Figure 4b, the minimum absorption energy is observed at a 30° orientation on the Al_2O_3 surface. Notably, an antiparallel angle of 90° emerges as the second most stable configuration, a finding that resonates with extant literature.[3f,16] By contrast, for MoS_2 on the Fe_2O_3 surface, the 0° alignment emerges as the most energetically favorable configuration across a full scan ranging from 0° to 120°, as shown in Figure 4c. It merits attention that achieving single orientation control of MoS_2 growth necessitates specific design considerations for steps on the Al_2O_3 surface. This is due to the mirror symmetry along the [11$\bar{2}$0]-plane, which culminates in a 30°/90° antiparallel growth.[6] Interestingly, the 0° alignment, which is thermodynamically favored on Fe_2O_3 surfaces, ensures that the mirror symmetry along the [11$\bar{2}$0]-plane will not lead to any antiparallel flake formation. This means we can achieve single orientation growth, even on surfaces with random steps. Reinforcing this hypothesis, the AFM image in Figure S8 (Supporting Information) evinces an absence of a regular step structure on Fe_2O_3-decorated sapphire surfaces, signifying that the unidirectional MoS_2 growth was guided by the exposed Fe_2O_3 surfaces by van der Waals epitaxy.

In the pursuit of feasible applications, achieving consistent single-orientation growth is critical. While the influence of the substrate surface is evident, growth conditions, including the metal-to-chalcogen ratio and temperature, also play a pivotal role in governing their orientation. For a comprehensive understanding, we systematically investigate the interdependence of temperature and Mo/S vapor supply ratio on orientation control using the Fe_2O_3-decorated sapphire substrate, as detailed in **Figure 5**. We began by placing the Fe_2O_3-decorated sapphire substrate in the central heating zones, and temperature parameters were adjusted between 675 and 775 °C to observe MoS_2 growth (refer to Figure 5a). Furthermore, with the central heating zone stabilized at 750 °C, MoS_2 growth profiles were captured from diverse substrate positions (as depicted in Figure 5b). Literature suggests a decreasing Mo/S vapor source ratio as the substrate's distance from the oxide precursors increases.[16b] Consequently, MoS_2 grown in the upstream region is characterized by a high Mo/S ratio, while the downstream region exhibits a diminished Mo/S ratio. Our observations align with prior research,[17] confirming that both temperature and Mo/S ratio substantially influence nucleation density, grain morphology, and size. However, the impact of these variables on growth orientation is comparatively muted on Fe_2O_3-decorated sapphire substrates, which is in clear contrast to previous observations.[8b,16b] Table S1 (Supporting Information) presents a statistical analysis of the single orientation percentages under various growth conditions. The percentages consistently remain above 95% in the temperature range of 675–775 °C. As the temperature increases, the percentage rises from 96.8% at 675 °C to 99% at 775 °C. Notably, at temperatures below 675 °C or subjected to extremely low Mo or S concentration, a transition in MoS_2 grains to dendritic morphology is observed (see Figures S9 and S10, Supporting Information), likely indicative of growth behavior dominated by kinetic controls.[18]

© 2023 The Authors. Advanced Functional Materials published by Wiley-VCH GmbH

16163028, 2024, 10, Downloaded from https://onlinelibrary.wiley.com/doi/10.1002/adfm.202311387, Wiley Online Library on [26/09/2024]. See the Terms and Conditions (https://onlinelibrary.wiley.com/terms-and-conditions) on Wiley Online Library for rules of use; OA articles are governed by the applicable Creative Commons License

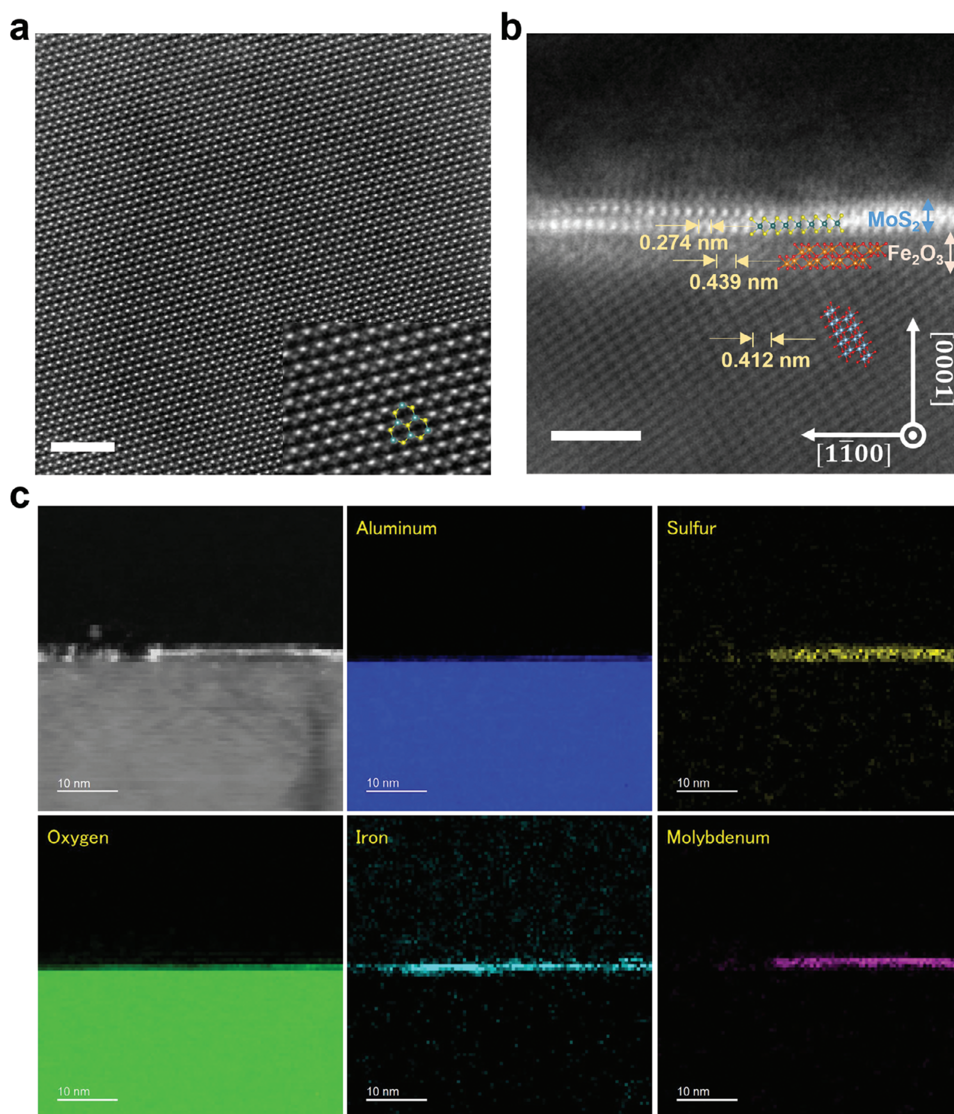

Figure 3. TEM images show the atomic structure of MoS_2 on Fe_2O_3-decorated sapphire. a) Top-view HAADF-STEM image of monolayer MoS_2 (scale bar: 2 nm). b) Cross-sectional HADDF-STEM image of MoS_2 grown on Fe_2O_3-decorated sapphire cut along [1$\bar{1}$00] (scale bar: 2 nm). c) EDX mapping of the cross-sectional STEM image for MoS_2 grown on Fe_2O_3-decorated sapphire.

Based on these findings, Fe_2O_3-decorated sapphire substrate offers robust reproducibility for single-orientation MoS_2 growth under a wide range of growth conditions.

Lastly, the back-gate field-effect transistors (FETs) were fabricated to illustrate the electrical properties of the as-grown single-oriented MoS_2. The schematic of back-gate MoS_2 FET is shown in **Figure 6a** with Bi/Au as the source/drain electrodes and 100 nm Si_3N_4 as the back-gate dielectric. 21 FET devices are shown in an array within 0.6×1 mm^2 area in the inset of Figure 6b. Figure 6b displays 50 transfer characteristic curves (drain-source current versus gate voltage, $I_{ds}-V_g$) with a channel length of 1.5 µm and channel width of 6.5 µm (as shown in Figure S11, Supporting Information), where the most on/off current ratios for the MoS_2 FETs achieve a high value of 10^7–10^8 at room temperature with V_{ds} of 1 V. In addition, minor on-state current variations and little subthreshold swing (SS) fluctuations suggest good uniformity of the MoS_2 grown on Fe_2O_3 decorated sapphire substrate. The output characteristics (drain-source current versus drain–source voltage, $I_{ds}-V_{ds}$, Figure 6c) show excellent ohmic contact features with promising current control and value, comparable to similar device configurations with Bi semimetal contact.[19] The average mobility of 50 devices was calculated as 12 cm^2 V^{-1} s^{-1}. Table S2 (Supporting Information) benchmarked the electrical properties of MoS_2 reported from the literature.[2b,3d,5,19,20] The mobility of the devices made from the MoS_2 grown on Fe_2O_3-decorated (0001) sapphire is comparable to other works. Additionally, the transfer characteristics of FETs made by MoS_2 grown on *c*-plane Fe_2O_3 and *c*-plane Al_2O_3 are compared, as shown in Figure 6d, where the transfer characteristics and achieved turn-on currents for both MoS_2 FETs are analogous. Furthermore, the threshold voltages (V_{th}) are −6.3 and −8.2 V, respectively. Several works indicate that V_{th} shifts obviously in strongly doped channel

© 2023 The Authors. Advanced Functional Materials published by Wiley-VCH GmbH

16163028, 2024, 10, Downloaded from https://onlinelibrary.wiley.com/doi/10.1002/adfm.202311387, Wiley Online Library on [26/09/2024]. See the Terms and Conditions (https://onlinelibrary.wiley.com/terms-and-conditions) on Wiley Online Library for rules of use; OA articles are governed by the applicable Creative Commons License

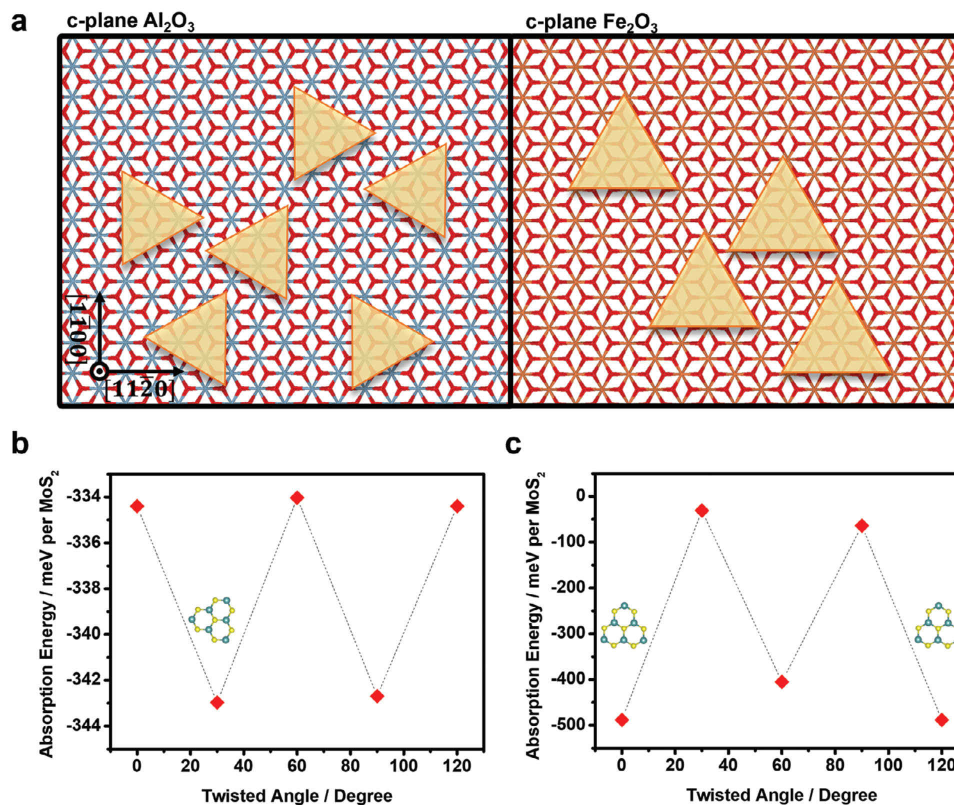

Figure 4. Reaction mechanism of single-oriented MoS_2. a) Schematic illustration comparing MoS_2 grown on Al_2O_3 (0001) and Fe_2O_3 (0001) surfaces. Adsorption energies as a function of the rotating MoS_2 monolayers resided on the b) Al_2O_3 (0001) and c) Fe_2O_3 (0001) surfaces.

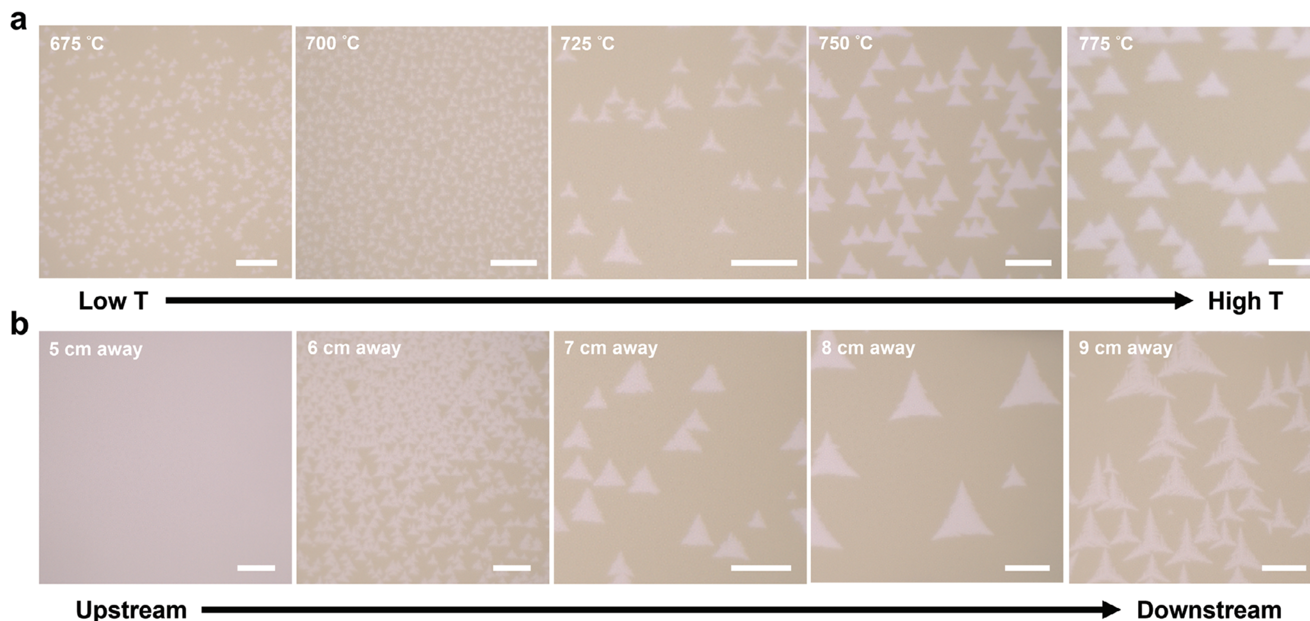

Figure 5. Single-oriented MoS_2 on Fe_2O_3-decorated sapphire at various growth conditions. a) OM images show single-oriented MoS_2 that was grown under various temperatures. b) OM images of MoS_2 grown at 750 °C from varying distances away from the MoO_3 precursor. (scale bar: 10 µm).

© 2023 The Authors. Advanced Functional Materials published by Wiley-VCH GmbH

16163028, 2024, 10, Downloaded from https://onlinelibrary.wiley.com/doi/10.1002/adfm.202311387, Wiley Online Library on [26/09/2024]. See the Terms and Conditions (https://onlinelibrary.wiley.com/terms-and-conditions) on Wiley Online Library for rules of use; OA articles are governed by the applicable Creative Commons License

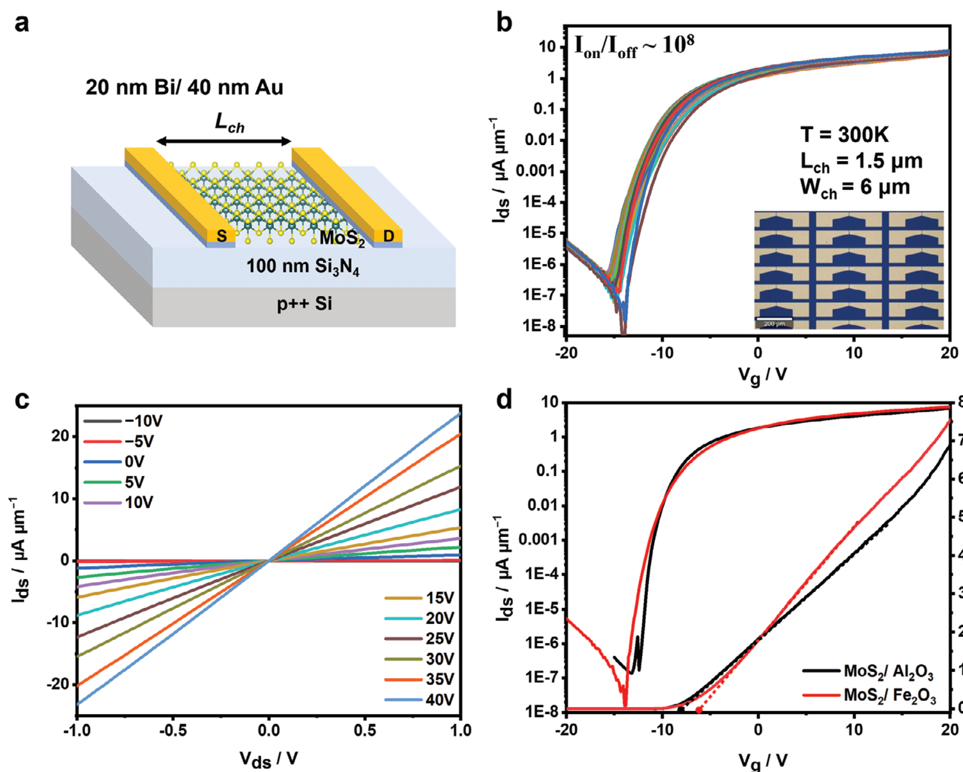

Figure 6. FET performance of single-crystal MoS_2. a) The schematic of MoS_2 FET devices. b) The transfer characteristics with $I_{ds}-V_g$ of 50 devices are shown in (a). c) Typical output curves of MoS_2 FET device from $V_g = -10$ V to 40 V with the increment of 5 V. d) Comparison of $I_{ds}-V_g$ characteristics for FETs with MoS_2 grown on c-plane sapphire and c-plane Fe_2O_3.

materials.[21] The resemblance in V_{th} implies a minimal variance in the electrical properties of MoS_2 grown on either substrate, which further suggests no significant doping side effect while adopting the Fe_2O_3-decorated substrate. These observations signify the reliability and reproducibility of the proposed approach.

3. Conclusion

In this work, we have effectively illuminated the potential of Fe_2O_3-decorated sapphire as a robust substrate for the epitaxial growth of 2D MoS_2. We identified that the MoS_2 orientation is governed by the symmetry of the topmost Fe_2O_3 crystal, diverging from the commonly observed step-edge guided growth. Through SHG mapping, it was affirmed that single-oriented MoS_2 flakes coalesce to form a continuous single crystal. Comprehensive characterizations using Raman and PL spectroscopies, along with HAADF-STEM imaging and EDX mapping, revealed the high quality of the MoS_2 film, with no apparent defects and doping concentration. Our DFT calculations underscored the crucial role of the Fe_2O_3 decoration layers, which ensure high reproducibility and consistency of single orientation growth, even on surfaces that present mirror-reflective challenges. Lastly, our fabricated back-gate MoS_2 FETs exhibited electrical performance on par with those cultivated on bare sapphires. Collectively, these findings shed light on achieving controlled MoS_2 orientation and epitaxy by manipulating crystalline atomic surfaces. This work offers a promising direction for those seeking scalable, high-quality, and reproducible methods for 2D TMD growth, holding significant implications for the next wave of electronic applications.

4. Experimental Section

Sapphire Treatment: C/M sapphires underwent an initial treatment by immersion in piranha solution (H_2O_2:H_2SO_4 = 1:3) for over 12 h. In the case of Fe_2O_3-decorated sapphire, the pretreated sapphires were subjected to spin-coating with a 20 μL solution of 0.5 μM $FeCl_2$ in ethanol. The influence of $FeCl_2$ concentration was discussed in the supporting information (Figure S12, Supporting Information). Subsequently, the substrates were heated to 1100 °C at a rate of 25 °C min^{-1} for a total duration of 8 h under an ambient atmosphere. For comparison, the pretreated C/M sapphires were similarly annealed under an ambient atmosphere at a temperature of 1100 °C with the same heating rate and duration.[2b,6,8b]

Growth of Single-Oriented MoS_2: The growth of MoS_2 was carried out using the LPCVD method at a pressure of 30 torr with a carrier gas flow rate of 80 sccm of argon (Ar).[2a] To initiate the growth process, ≈1 g of sulfur powder was positioned upstream of the reaction tube and heated to 160 °C, which was ≈7 cm away from the heating zone. Simultaneously, a quartz boat containing 150 mg of MoO_3 powder was placed 7 cm upstream from the centered heating zone at a temperature of 750 °C. This arrangement allowed for a growth time of 10 min to facilitate the formation of MoS_2. Fe_2O_3-decorated sapphire substrates were placed in the vicinity of ≈750 °C. For comparison purposes, the substrate zone of the furnace was heated to 725 °C, and undecorated sapphire substrates were placed at the center of this zone to undergo growth for a duration of 10 min.

Transfer of MoS_2 Film: The as-grown MoS_2 substrates were mildly attached to the polydimethylsiloxane (PDMS) polymer films. Subsequently, the substrates were immersed in 1 M NaOH aqueous solution. After the PDMS films were peeled off from the surface, the PDMS films were rinsed

© 2023 The Authors. Advanced Functional Materials published by Wiley-VCH GmbH

16163028, 2024, 10, Downloaded from https://onlinelibrary.wiley.com/doi/10.1002/adfm.202311387, Wiley Online Library on [26/09/2024]. See the Terms and Conditions (https://onlinelibrary.wiley.com/terms-and-conditions) on Wiley Online Library for rules of use; OA articles are governed by the applicable Creative Commons License

with DI water twice. Then, the PDMS films were pasted to the glass slide and mildly transferred to the target substrate at the rate of 2 µm s^{-1} by the E1-M transfer machine from METATEST Corporation.[22]

Back-Gate Device Fabrication: Monolayer MoS_2 was first transferred onto 100 nm Si_3N_4/p^{++}-Si substrates by the transfer mentioned above. The LED lithography was subsequently conducted to pattern 1.5 µm-long channel length. Following the thermal evaporation and 1-methyl-2-pyrrolidone (NMP) lift-off process, Bi and Au were deposited as the source/drain. The channels were defined by O_2 plasma reaching 6.5 µm channel width. All electrical properties were measured under high vacuum environments (<10^{-6} torr) with a Lakeshore probe station and a Keysight B1500A Semiconductor Device Parameter Analyzer. The mobilities of the monolayer MoS_2 were calculated through the equation: $\mu = (dI_{ds}/dV_g) \times [L_{ch}/(WC_{ox}V_{ds})]$, where I_{ds} is the drain current, V_g is the gate voltage, L_{ch} is the channel length, W is the channel width, C_{ox} represents the capacitance per unit area of the gate dielectric (7.00×10^{-4} F cm^{-2} for 100 nm Si_3N_4), and V_{ds} indicates the voltage between the source/drain.

Simulation Method: All calculations were performed using the Vienna Ab Initio Simulation Package (VASP) version 5.4.4 with the plane–wave basis set and projector-augmented wave (PAW) pseudopotential.[23] The Perdew–Burke–Ernzerhof (PBE) exchange–correlation function was employed to describe the electronic exchange and correlation effects.[24] The plane wave basis set energy cutoff was set to 520 eV. The Grimme's D3 correction was also included to account for the dispersion interactions.[25] The ionic relaxation was performed until the forces on each atom were less than 0.02 eV Å^{-1}. The electronic self-consistent field was calculated until the change in the total energy was less than 10^{-6} eV. The Brillouin zone sampling was restricted to only Gamma point due to the limited computational resources and enormously large system size. The DFT+U method was utilized to treat the localized Fe d-electrons, with a U value of 5.3 eV for Fe, as recommended by prior studies.[26]

The adsorption energy between monolayer MoS_2 on the Fe_2O_3 buffer layer was calculated using the following formula:

$$E_{ads} = \frac{E_{MoS_2/Fe_2O_3} - E_{MoS_2} - E_{Fe_2O_3}}{N_{MoS_2}} \quad (1)$$

where E_{MoS_2/Fe_2O_3} is the total energy of the heterojunction system comprising MoS_2 adsorbed on the Fe_2O_3 buffer layer, E_{MoS_2} is the total energy of the isolated MoS_2 monolayer, $E_{Fe_2O_3}$ is the total energy of the individual Fe_2O_3 buffer layer, and N_{MoS_2} is the number of MoS_2 units of MoS_2 monolayer in heterojunction system. The Fe_2O_3 buffer layer was modeled using a slab model, and the MoS_2 monolayer was placed on top of the Fe_2O_3 slab. To prevent spurious interactions from periodic images, a vacuum layer with a thickness of at least 12 Å was included in the system. All energies were calculated using the same computational parameters as described above.

TEM/ STEM Characterizations: The cross-sectional STEM sample was first prepared with a focused ion beam (FIB). A dual-beam FIB-SEM system (Versa3D, FEI) was employed to create thin samples. Before FIB thinning, MoS_2 samples received SiO_2 protective coating via electron gun, followed by Au deposition to enhance conductivity and prevent charging. The MoS_2 sample was oriented for planar milling, with the milling direction perpendicular to the $(1\bar{1}00)$ plane direction, which aligns with the TEM/STEM zone axis. Specifically, milling occurred along the height direction of the MoS_2 equilateral triangle. For STEM samples, extensive preparation was needed to achieve the necessary thinness. A Ga^+ beam acceleration voltage of 30 kV was used, with Ga^+ beam currents ranging from 75−1300 pA for milling.

A JEOL JEM-ARM200F TEM with a Corrected Electron Optical Systems (CEOS) probe spherical aberration corrector was utilized, operating at 80–200 keV. The vacuum level during measurements was $\approx 1.3 \times 10^{-7}$ mbar, while the electron beam current maintained a value of 13.1 µA. STEM imaging employed a camera length of 120 mm and a defocus of ≈−4 nm. Image acquisition involved capturing high-angle annular dark field (HAADF) images at a rate of 19 µs per pixel, with all images sized at 1024 × 1024 pixels. The condenser lens aperture measured 40 µm, with a collection angle range spanning from 45 to 180 mrad. To enhance image quality, Wiener filtering was applied to the HAADF images in the filtered set, effectively reducing noise interference.

Characterizations of MoS_2: Single-oriented MoS_2 was further characterized by SEM (LEO 1530 FEG-SEM) and AFM (Dimension Icon, Bruker). Raman, PL, and SHG spectra were collected by WITec alpha300R with the laser source of 488 and 1064 nm and a×100 objective lens (NA, 0.9). XPS was operated at the TLS beamline 24A1 at the National Synchrotron Radiation Research Center (NSRRC), Hsinchu, Taiwan.

Supporting Information

Supporting Information is available from the Wiley Online Library or from the author.

Acknowledgements

L.J.L thanks the support from the Jockey Club Hong Kong to the JC STEM lab of 3DIC (2022-0118) and the Research Grant of the Council of Hong Kong (CRS_PolyU502/22). Y. W. & L.J.L acknowledge the support from the University of Hong Kong and the National Key R&D Project of China (2022YFB4044100).

Conflict of Interest

The authors declare no conflict of interest.

Author Contributions

Y.-M.C. and N.Y. contributed equally to the work. Y.W. conceived the project. Y.-M.C. and B.Y. operated the decoration of sapphire. Y.-M.C., P.Y., Y.Z., C.L., and B.Y. synthesized and transferred MoS_2. Y.-M.C., N.Y., and J.-B.X. completed the AFM analyses. N.Y. and J.-K.H. accomplished the FETs fabrication and electrical measurements. J.M. and K.S. carried out the first-principles calculations. F.Z., C.-W.H., J.-Y.C., Z.L., and W.-W.W. conducted the TEM/STEM characterizations. H-Y.L. and H-Y.C. executed XPS analyses. Raman, PL, SHG, and SEM were done by Y.-M.C. All the authors contributed to the results and discussions. Y.-M.C., L.-J.L., and Y.W. wrote the paper.

Data Availability Statement

The data that support the findings of this study are available from the corresponding author upon reasonable request.

Keywords

chemical vapor deposition, molybdenum disulfide, orientation control, single crystal, transition metal dichalcogenide

Received: September 19, 2023
Revised: October 22, 2023
Published online: November 29, 2023

[1] a) M.-Y. Li, S.-K. Su, H.-S. P. Wong, L.-J. Li, *Nature* **2019**, *567*, 169; b) Z. Sun, C.-S. Pang, P. Wu, T. Y. T. Hung, M.-Y. Li, S. L. Liew, C.-C. Cheng, H. Wang, H.-S. P. Wong, L.-J. Li, I. Radu, Z. Chen, J. Appenzeller, *ACS Nano* **2022**, *16*, 14942; c) J.-K. Huang, J. Pu, C.-L. Hsu, M.-H. Chiu, Z.-Y. Juang, Y.-H. Chang, W.-H. Chang, Y. Iwasa, T. Takenobu, L.-J. Li, *ACS Nano* **2014**, *8*, 923.

© 2023 The Authors. Advanced Functional Materials published by Wiley-VCH GmbH

16163028, 2024, 10, Downloaded from https://onlinelibrary.wiley.com/doi/10.1002/adfm.202311387, Wiley Online Library on [26/09/2024]. See the Terms and Conditions (https://onlinelibrary.wiley.com/terms-and-conditions) on Wiley Online Library for rules of use; OA articles are governed by the applicable Creative Commons License

[2] a) Y.-H. Lee, X.-Q. Zhang, W. Zhang, M.-T. Chang, C.-T. Lin, K.-D. Chang, Y.-C. Yu, J. T.-W. Wang, C.-S. Chang, L.-J. Li, T.-W. Lin, *Adv. Mater.* **2012**, *24*, 2320; b) T. Li, W. Guo, L. Ma, W. Li, Z. Yu, Z. Han, S. Gao, L. Liu, D. Fan, Z. Wang, Y. Yang, W. Lin, Z. Luo, X. Chen, N. Dai, X. Tu, D. Pan, Y. Yao, P. Wang, Y. Nie, J. Wang, Y. Shi, X. Wang, *Nat. Nanotechnol.* **2021**, *16*, 1201; c) J. Wang, X. Xu, T. Cheng, L. Gu, R. Qiao, Z. Liang, D. Ding, H. Hong, P. Zheng, Z. Zhang, Z. Zhang, S. Zhang, G. Cui, C. Chang, C. Huang, J. Qi, J. Liang, C. Liu, Y. Zuo, G. Xue, X. Fang, J. Tian, M. Wu, Y. Guo, Z. Yao, Q. Jiao, L. Liu, P. Gao, Q. Li, R. Yang, et al., *Nat. Nanotechnol.* **2021**, *17*, 33; d) T.-A. Chen, C.-P. Chuu, C.-C. Tseng, C.-K. Wen, H.-S. P. Wong, S. Pan, R. Li, T.-A. Chao, W.-C. Chueh, Y. Zhang, Q. Fu, B. I. Yakobson, W.-H. Chang, L.-J. Li, *Nature* **2020**, *579*, 219.

[3] a) P. Yang, F. Liu, X. Li, J. Hu, F. Zhou, L. Zhu, Q. Chen, P. Gao, Y. Zhang, *Small Methods* **2023**, *7*, 2300165; b) A. Aljarb, J. Min, M. Hakami, J.-H. Fu, R. Albaridy, Y. Wan, S. Lopatin, D. Kaltsas, D. Naphade, E. Yengel, *ACS Nano* **2023**, *17*, 10010; c) L. Liu, T. Li, L. Ma, W. Li, S. Gao, W. Sun, R. Dong, X. Zou, D. Fan, L. Shao, C. Gu, N. Dai, Z. Yu, X. Chen, X. Tu, Y. Nie, P. Wang, J. Wang, Y. Shi, X. Wang, *Nature* **2022**, *605*, 69; d) J. Hu, W. Quan, P. Yang, F. Cui, F. Liu, L. Zhu, S. Pan, Y. Huan, F. Zhou, J. Fu, G. Zhang, P. Gao, Y. Zhang, *ACS Nano* **2022**, *17*, 312; e) P. Yang, D. Wang, X. Zhao, W. Quan, Q. Jiang, X. Li, B. Tang, J. Hu, L. Zhu, S. Pan, Y. Shi, Y. Huan, F. Cui, S. Qiao, Q. Chen, Z. Liu, X. Zou, Y. Zhang, *Nat. Commun.* **2022**, *13*, 3238; f) P. Zheng, W. Wei, Z. Liang, B. Qin, J. Tian, J. Wang, R. Qiao, Y. Ren, J. Chen, C. Huang, X. Zhou, G. Zhang, Z. Tang, D. Yu, F. Ding, K. Liu, X. Xu, *Nat. Commun.* **2023**, *14*, 592.

[4] X. Li, J. Yang, H. Sun, L. Huang, H. Li, J. Shi, *Adv. Mater.* **2023**, 2305115.

[5] P. Yang, S. Zhang, S. Pan, B. Tang, Y. Liang, X. Zhao, Z. Zhang, J. Shi, Y. Huan, Y. Shi, S. J. Pennycook, Z. Ren, G. Zhang, Q. Chen, X. Zou, Z. Liu, Y. Zhang, *ACS Nano* **2020**, *14*, 5036.

[6] J.-H. Fu, J. Min, C.-K. Chang, C.-C. Tseng, Q. Wang, H. Sugisaki, C. Li, Y.-M. Chang, I. Alnami, W.-R. Syong, *Nat. Nanotechnol.* **2023**, *18*, 1289.

[7] D. Ding, S. Wang, Y. Xia, P. Li, D. He, J. Zhang, S. Zhao, G. Yu, Y. Zheng, Y. Cheng, M. Xie, F. Ding, C. Jin, *ACS Nano* **2022**, *16*, 17356.

[8] a) A. Cohen, P. K. Mohapatra, S. Hettler, A. Patsha, K. V. L. V. Narayanachari, P. Shekhter, J. Cavin, J. M. Rondinelli, M. Bedzyk, O. Dieguez, R. Arenal, A. Ismach, *ACS Nano* **2023**, *17*, 5399; b) Y. Park, C. Ahn, J.-G. Ahn, J. H. Kim, J. Jung, J. Oh, S. Ryu, S. Kim, S. C. Kim, T. Kim, H. Lim, *ACS Nano* **2023**, *17*, 1196; c) Y.-C. Lin, B. Jariwala, B. M. Bersch, K. Xu, Y. Nie, B. Wang, S. M. Eichfeld, X. Zhang, T. H. Choudhury, Y. Pan, R. Addou, C. M. Smyth, J. Li, K. Zhang, M. A. Haque, S. Fölsch, R. M. Feenstra, R. M. Wallace, K. Cho, S. K. Fullerton-Shirey, J. M. Redwing, J. A. Robinson, *ACS Nano* **2018**, *12*, 965; d) Y. Xiang, X. Sun, L. Valdman, F. Zhang, T. H. Choudhury, M. Chubarov, J. A. Robinson, J. M. Redwing, M. Terrones, Y. Ma, L. Gao, M. A. Washington, T.-M. Lu, G.-C. Wang, *2D Mater.* **2020**, *8*, 025003.

[9] A. P. Grosvenor, B. A. Kobe, M. C. Biesinger, N. S. Mcintyre, *Surf. Interface Anal.* **2004**, *36*, 1564.

[10] a) X. Yin, Z. Ye, D. A. Chenet, Y. Ye, K. O'brien, J. C. Hone, X. Zhang, *Science* **2014**, *344*, 488; b) J. Cheng, T. Jiang, Q. Ji, Y. Zhang, Z. Li, Y. Shan, Y. Zhang, X. Gong, W. Liu, S. Wu, *Adv. Mater.* **2015**, *27*, 4069.

[11] J.-H. Park, A.-Y. Lu, P.-C. Shen, B. G. Shin, H. Wang, N. Mao, R. Xu, S. J. Jung, D. Ham, K. Kern, Y. Han, J. Kong, *Small Methods* **2021**, *5*, 2000720.

[12] H. W. Wang, P. Skeldon, G. E. Thompson, *Surf. Coat. Technol.* **1997**, *91*, 200.

[13] a) H. Li, J. Yang, X. Li, Q. Luo, M. Cheng, W. Feng, R. Du, Y. Wang, L. Song, X. Wen, Y. Wen, M. Xiao, L. Liao, Y. Zhang, J. Shi, J. He, *Adv. Mater.* **2023**, *35*, 2211536; b) H. Li, M. Cheng, P. Wang, R. Du, L. Song, J. He, J. Shi, *Adv. Mater.* **2022**, *34*, 2200885.

[14] a) J. Wu, S. Mao, Z.-G. Ye, Z. Xie, L. Zheng, *ACS Appl. Mater. Interfaces* **2010**, *2*, 1561; b) A. Lassoued, B. Dkhil, A. Gadri, S. Ammar, *Results Phys.* **2017**, *7*, 3007.

[15] X.-G. Wang, A. Chaka, M. Scheffler, *Phys. Rev. Lett.* **2000**, *84*, 3650.

[16] a) D. Dumcenco, D. Ovchinnikov, K. Marinov, P. Lazic, M. Gibertini, N. Marzari, O. L. Sanchez, Y.-C. Kung, D. Krasnozhon, M.-W. Chen, S. Bertolazzi, P. Gillet, A. Fontcuberta I Morral, A. Radenovic, A. Kis, *ACS Nano* **2015**, *9*, 4611; b) A. Aljarb, Z. Cao, H.-L. Tang, J.-K. Huang, M. Li, W. Hu, L. Cavallo, L.-J. Li, *ACS Nano* **2017**, *11*, 9215.

[17] J. Xu, D. J. Srolovitz, D. Ho, *ACS Nano* **2021**, *15*, 6839.

[18] J. Wang, X. Cai, R. Shi, Z. Wu, W. Wang, G. Long, Y. Tang, N. Cai, W. Ouyang, P. Geng, B. N. Chandrashekar, A. Amini, N. Wang, C. Cheng, *ACS Nano* **2018**, *12*, 635.

[19] P.-C. Shen, C. Su, Y. Lin, A.-S. Chou, C.-C. Cheng, J.-H. Park, M.-H. Chiu, A.-Y. Lu, H.-L. Tang, M. M. Tavakoli, G. Pitner, X. Ji, Z. Cai, N. Mao, J. Wang, V. Tung, J. Li, J. Bokor, A. Zettl, C.-I. Wu, T. Palacios, L.-J. Li, J. Kong, *Nature* **2021**, *593*, 211.

[20] a) H. Liu, Q. H. Thi, P. Man, X. Chen, T. Chen, L. W. Wong, S. Jiang, L. Huang, T. Yang, K. H. Leung, T. T. Leung, S. Gao, H. Chen, C.-S. Lee, M. Kan, J. Zhao, Q. Deng, T. H. Ly, *Adv. Mater.* **2023**, *35*, 2210503; b) A. M. Van Der Zande, P. Y. Huang, D. A. Chenet, T. C. Berkelbach, Y. You, G.-H. Lee, T. F. Heinz, D. R. Reichman, D. A. Muller, J. C. Hone, *Nat. Mater.* **2013**, *12*, 554.

[21] a) L. Yang, K. Majumdar, H. Liu, Y. Du, H. Wu, M. Hatzistergos, P. Y. Hung, R. Tieckelmann, W. Tsai, C. Hobbs, P. D. Ye, *Nano Lett.* **2014**, *14*, 6275; b) A. Tarasov, S. Zhang, M.-Y. Tsai, P. M. Campbell, S. Graham, S. Barlow, S. R. Marder, E. M. Vogel, *Adv. Mater.* **2015**, *27*, 1175.

[22] S. Tongay, W. Fan, J. Kang, J. Park, U. Koldemir, J. Suh, D. S. Narang, K. Liu, J. Ji, J. Li, R. Sinclair, J. Wu, *Nano Lett.* **2014**, *14*, 3185.

[23] a) G. Kresse, J. Furthmüller, *Phys. Rev. B* **1996**, *54*, 11169; b) G. Kresse, D. Joubert, *Phys. Rev. B* **1999**, *59*, 1758.

[24] J. P. Perdew, K. Burke, M. Ernzerhof, *Phys. Rev. Lett.* **1996**, *77*, 3865.

[25] S. Grimme, J. Antony, S. Ehrlich, H. Krieg, *J. Chem. Phys.* **2010**, *132*, 154104.

[26] A. Jain, S. P. Ong, G. Hautier, W. Chen, W. D. Richards, S. Dacek, S. Cholia, D. Gunter, D. Skinner, G. Ceder, *APL Mater.* **2013**, *1*, 011002.

© 2023 The Authors. Advanced Functional Materials published by Wiley-VCH GmbH

16163028, 2024, 10, Downloaded from https://onlinelibrary.wiley.com/doi/10.1002/adfm.202311387, Wiley Online Library on [26/09/2024]. See the Terms and Conditions (https://onlinelibrary.wiley.com/terms-and-conditions) on Wiley Online Library for rules of use; OA articles are governed by the applicable Creative Commons License